A derivative-based fast autofocus method

EINDHOVEN UNIVERSITY OF TECHNOLOGY
Department of Mathematics and Computer Science

CASA-Report 11-13
February 2011

A derivative-based fast autofocus method

by

M.E. Rudnaya, H.G. ter Morsche,
J.M.L. Maubach, R.M.M. Mattheij

Centre for Analysis, Scientific computing and Applications
Department of Mathematics and Computer Science
Eindhoven University of Technology
P.O. Box 513
5600 MB Eindhoven, The Netherlands
ISSN: 0926-4507

A derivative-based fast autofocus method

M.E. Rudnaya, H.G. ter Morsche, J.M.L. Maubach, R.M.M. Mattheij

Abstract

Most automatic focusing methods are based on a sharpness function, which delivers a real-valued estimate of an image quality. In this paper, we study an L_2-norm derivative-based sharpness function, which has been used before based on heuristic consideration. We give a more solid mathematical foundation for this function and get a better insight into its analytical properties. Moreover an efficient autofocus method is presented, in which an artificila blur variable plays an important role.

We show that for a specific choice of the artificial blur control variable, the function is approximately a quadratic polynomial, which implies that after obtaining of at least three images one can find the approximate position of the optimal defocus. This provides the speed improvement in comparison with existing approaches, which usually require recording of more than ten images for autofocussing. The new autofocus method is employed for the scanning transmission electron microscopy. To be more specific, it has been implemented in the FEI scanning transmission electron microscope and its performance has been tested as a part of a particle analysis application.

1 Introduction

Consider an optical device, such as a photocamera, a telescope or a microscope. An image obtained with the optical device depends on a given object's geometry, known as the *object function*, and the optical device *defocus*. The method of automatic defocus determination, such that the recorded image has the highest possible quality (the image is *in-focus*), is known as *automated focusing* or *autofocus* method.

The existing autofocus methods used for different types of optical devices are usually based on a *sharpness function*, a real-valued estimate of the image's sharpness. For a through-focus series an ideal sharpness function should reach a single optimum (maximum or minimum, depending on a sharpness function definition) at the in-focus image. Existing sharpness functions are based on the image derivatives [1, 21, 35], variance [4, 28], autocorrelation [9, 22, 34], histogram [14, 36] or Fourier transform [11, 27, 31, 33]. An overview of existing sharpness functions can be found in [16, 27, 29, 36].

An autofocus method can be established in two different ways:

- A number of images is taken within a wide defocus range and for each image the sharpness function is computed giving a discrete set of sharpness function values . Then the optimal image (the in-focus image) is determined as the optimum of this discrete set of data (course focusing). Eventually the same procedure is repeated within a smaller defocus range around the optimum, found on the previous step (fine focusing).

- Starting out with an initial defocus parameter d, an iterative optimization method is used to find the optimal defocus value d_0, (for example, Fibbonachi search [16, 36], Nelder-Mead simplex method [28] or Powell interpolation-based trust-region method [25]).

The first approach requires recording of about 20-30 images, which can be time-consuming for real-world applications. The goal of the second approach is to minimize the number of images necessary to perform the autofocus. It usually requires not less than 10 images for the autofocus procedure.

In literature a number of sharpness functions has been considered and discussed for different optical devices, such as photographic and video cameras [5, 11, 14], telescopes [19, 12], light microscopes [1, 9, 16, 29, 30, 35, 36] and electron microscopes [4, 22, 26, 27, 31, 33]. In this paper use the electron microscopy as a reference application for our autofocus method. To be more precise, the experimental application is tested for low resolution *scanning transmission electron microscopy (STEM).*

For many practical applications in STEM, defocus has to be adjusted regularly during the continuous image recording process. For instance, in electron tomography 50-100 images are recorded at different tilt angles, where each tilting changes the defocus [33]. Other possible reasons for change in defocus are for instance the instabilities of the electron microscope and environment, as well as the magnetic nature of some samples. The capacity of the modern processors allows computations of a sharpness function within a negligible amount of time. However, image recording might require a noticeable amount of time. In particularly in STEM, one image recording can take 1-to 10 seconds. For this reason the development of a method that requires fewer images is important. A number of methods implemented on aberrated-corrected electron microscopes are able to correct high and low aberrations including defocus [17, 8, 37]. For defocus correction these methods require from one to four images only. However they are based on specific assumptions about the object geometry. These methods are not suitable for applications that require continuous operation since they are not fully autonomous [32]. In addition some of them make use of additional equipment, such as aberration correctors or a special camera, which is not a part of every microscope.

In this paper we study derivative-based sharpness functions. The advantage of using these functions has been already shown experimentally for scanning electron microscopy images [26, 27]. Some of them are based on a L_2-norm of an image derivative [1, 14, 36]. The use of these functions is heuristic in nature. Usually they are based on the assumption that the in-focus image has a larger difference between neighboring pixels than the defocused one. In this paper we show analytically that for the noise-free image formation the L_2-norm derivative-based sharpness function reaches its optimum for the in-focus image, and does not have any other optima. Moreover under certain assumptions the function can accurately be approximated by a quadratic polynomial. The error of this approximation can be decreased be adjusting the artificial blur control variable, which is given as an input to the autofocus method. The proposed quadratic polynomial interpolation leads to a new autofocus method that requires recording of three or four images only. The method is implemented in FEI STEM and is demonstrated for a real-world microscopy application.

The paper is set up as follows: Section 2 explains the image formation modelling used in this paper. Section 3 provides the definition of the derivative-based sharpness function, and explains the process of automated focussing. In Section 4 theoretical observations on derivative-based sharpness function are given. Subsequently Section 5 describes the quadratic interpolation of the sharpness function and the autofocus method. Numerical computations for experimental data obtained from a STEM FEI microscope are shown in Section 6. Section 7 presents the results of the on-line autofocus correction method implemented and running on a FEI STEM prototype. Finally Section 8 provides discussion on relationship between the mathematical theory and real-world applications.

2 Modelling

Usually an image is two-dimensional. However for the simplification of our analysis we restrict the theoretical observations to a one-dimensional setting. If the objective lens of the optical device is rotationally symmetric, this restriction does not affect the real problem, because the two-dimensional case in image formation is a repetition of the one-dimensional case in an orthogonal direction. Nevertheless, in our numerical experiments and the real-world application (sections 6-7) two-dimensional images are used. One of the experiments will correspond to the situation of the non-symmetric lens (for instance, the lens with *astigmatism* abberation).

The Fourier transform $\hat{f}$ of a function $f \in \mathrm{L}^2(\mathbb{R})$ plays a fundamental role in our analysis and modeling. It is defined as follows

$$\hat{f}(\omega) = \int_{-\infty}^{\infty} f(x) e^{-\mathrm{i}\omega x} \mathrm{d}x,$$

where x is a *spatial coordinate* and ω is a *frequency coordinate*.

Images for which our sharpness function will be computed are the output images f of the so-called image formation model represented by Figure 1. The object's geometry (or the *object function*) is denoted by ψ. The filter ϱ_σ in Figure 1 describes the *point spread function* of an optical device. The point spread function can accurately be approximated by a *Lévi stable density* function for a wide class of optical devices [2, 3, 10]. The Lévi stable density function is implicitly defined via its Fourier transform as follows

$$\hat{\varrho}_\sigma(\omega) := e^{-\frac{\sigma^2 \omega^{2\beta}}{2}}, \quad 0 < \beta \leq 1. \tag{1}$$

The parameter β in (1) depends on the optical device, and σ in (1) is known as the *width* of the point spread function. It is simply related to the control variable d, i.e. the defocus of the optical device

$$\sigma = d - d_0,$$

where d_0 is unknown. The goal of the autofocus procedure is to find the value of d_0.

The output of the ϱ_σ filter is denoted by f_0 and often post-processed by a PC, cf. Figure 1. In our model we assume that in such post-processing a Gaussian filter is applied to the image f_0

$$g_\alpha(x) := \frac{1}{\sqrt{2\pi}\alpha} e^{-\frac{x^2}{2\alpha^2}}.$$

Filtering with a Gaussian kernel is often applied for denoising purposes, which is an easy alternative to more advanced denoising techniques [15, 18, 24]. In our autofocus procedure the main use of the control variable α is not for denoising the image f_0. As explained in the following sections, it influences the approximation error when the sharpness function is replaced by a quadratic polynomial, but it does not change the location of d_0. The value of the

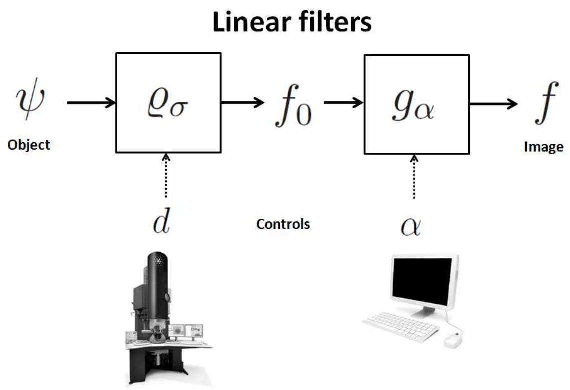

Figure 1: The image formation model.

control variable α is fixed during the autofocus process; i.e. when we attempt to find d_0 from a number of recorded images corresponding to different values of d stemming from the same object function ψ.

We apply the *linear image formation model*, which is often used for various optical devices [2, 7, 21, 38], in particular for electron microscopes [4, 13]. This implies that the occurring filters are linear and space invariant which easily can be described by means of convolution products

$$f_0 := \psi * \varrho_\sigma, \quad f := f_0 * g_\alpha. \tag{2}$$

If no image post-processing is applied then, $\alpha = 0$, and $f = f_0$.

3 Sharpness function and problem formulation

In this section we introduce the derivative-based sharpness function explicitly and investigate its behaviour with respect to the defocus parameter d. As the parameter d is closely related to the width σ it is convenient to define the sharpness function as a function of σ as (cf.[14, 16])

$$\Lambda(\sigma) := \| \frac{\partial}{\partial x} f \|^2_{L_2}. \tag{3}$$

For the linear image formation model (2), we have

$$\Lambda(\sigma) := \| \frac{\partial}{\partial x} (\psi * \varrho_\sigma * g_\alpha) \|^2_{L_2}. \tag{4}$$

Since $\sigma = d - d_0$, we will consider the function $\Lambda(d - d_0)$. For a through-focus series of images the sharpness function is computed at different values of d for a fixed value of α. A general behaviour of a sharpness function is shown in Figure 2. The image at the defocus $d = d_0$ is sharp or *in-focus* and the sharpness function reaches its optimum. The image far away from d_0 is called *out-of-focus*.

We recall that for our autofocus procedure α is fixed and a finite number, say N, of the defocus control d are chosen: $d_1, \ldots, d_N$ with $d_1 < d_2 < \ldots < d_N$. For each of the corresponding images $f_1, f_2, \ldots, f_N$ the value of a sharpness function is computed

$$\Lambda_i := \Lambda(d_i - d_0), \quad i = 1, \ldots, N \tag{5}$$

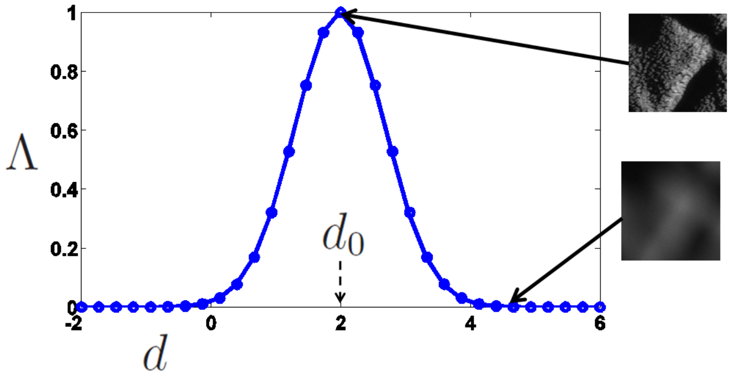

Figure 2: Sharpness function F reaches its optimum at the in-focus image. The goal of the autofocus procedure is to find the value of defocus d_0.

As already mentioned before, the problem of automated focussing is to estimate the optimum location d_0 of the sharpness function from the given points (5). The location d_0 is independent on the object function ψ.

In this paper our aim is to do this using a small number of recorded images, i.e., $N = 3$ or $N = 4$, while in other papers $N > 10$ is usually used [14, 16, 36, 38]. For this purpose we will look for the function shape which can be accurately approximated by a quadratic polynomial. In the next section the error estimates of such an approximation for derivative-based sharpness function are provided.

4 Theoretical observations

In this section we collect some useful properties of the derivative based sharpness function. First, in Subsection 4.1, we deal with general properties of Λ in case the spread function ϱ_σ is a Lévi stable density function function. In Subsection 4.2, we restrict ourselves to the Gaussian point spread functions and study in more detail properties of Λ for a typical collection of object functions: A Gaussian particle and the more general case of a digital image.

4.1 General properties of the sharpness function Λ

Property 1. *If f is given by the linear image formation model (2) then the sharpness function Λ is*

$$\Lambda(\sigma) = \frac{1}{2\pi} \int_{-\infty}^{\infty} \omega^2 |\hat{\psi}(\omega)|^2 e^{-\sigma^2\omega^{2\beta}} e^{-\alpha^2\omega^2} \, d\omega. \tag{6}$$

Proof. For $\hat{\psi}, \hat{g}, \hat{f}$, the Fourier transforms of ψ, g, f respectively, it holds that $\hat{f} = \hat{\psi}\hat{\varrho}_\sigma\hat{g}_\alpha$. Then because of Parseval's identity one has

$$\Lambda(\sigma) := \|\frac{\partial}{\partial x} f\|_{L^2}^2 = \frac{1}{2\pi}\|\omega \hat{f}\|_{L^2}^2 = \frac{1}{2\pi}\int_{-\infty}^{\infty} \omega^2 |\hat{\psi}(\omega)|^2 |\hat{\varrho}_\sigma(\omega)|^2 |\hat{g}_\alpha(\omega)|^2 \mathrm{d}\omega.$$

$\square$

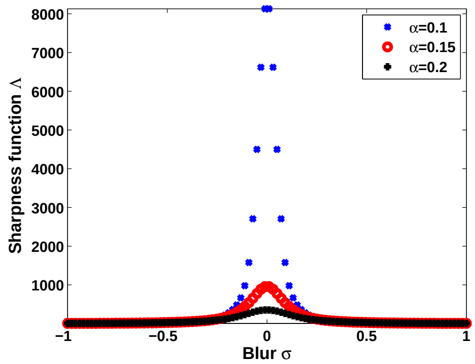

Figure 3: Numerically computed sharpness functions Λ.

We assume that the object function satisfies the property

$$\int_{-\infty}^{\infty} |\psi(x)| \mathrm{d}x < \infty, \tag{7}$$

which holds throughout the paper. In practice this property will be easily satisfied because the function ψ has a finite domain, i.e., the image has a finite size. As a consequence we have that $\hat{\psi}$ is bounded and continuous. In case of a digital image (cf. Subsection 4.2) having a finite number of pixels, $\hat{\psi}$ is a tri-geometric polynomial which again is bounded and smooth.

Property 2. *For the object function (7), the sharpness function $\Lambda(\sigma)$ is smooth, and is strictly increasing for $\sigma < 0$ and strictly decreasing for $\sigma > 0$.*

Property 3. *For the object function (7) and $\alpha > 0$, the sharpness function $\Lambda(\sigma)$ has a finite maximum at $\sigma = 0$*

$$\max_{\sigma} \Lambda(\sigma) = \Lambda(0).$$

The properties 2-3 follow directly from (6). Figure 3 shows a numerically computed sharpness functions Λ for different values of α.

Due to the physical limitations of the optical device the width of the point spread function has a positive underbound: $\sigma > \sigma_0$ for a certain positive number σ_0. From now on, we consider a Gaussian point spread function, i.e. $\beta = 1$ in (1). A Gaussian function (or a composition of Gaussian functions) is often used as an approximation of the point spread function for different optical devices [18, 21, 38], including the electron microscopes [4, 20].

As a special example of a sharpness function, we deal with an object function for which the power spectrum corresponds to a Gaussian function. Such images often occur in experimental images from single particles. In our one-dimensional setting we may therefore assume that

$$|\hat{\psi}(\omega)|^2 = Ce^{-\omega^2\gamma^2}, \quad C > 0, \quad \gamma \geq 0. \tag{8}$$

For $\gamma = 0$ in (8), $|\hat{\psi}|^2$ is a constant, which corresponds to the situation when the object is nearly *amorphous* [4].

Property 4. *For the object function (8) and a Gaussian point spread function it follows*

$$\Lambda(\sigma) = \frac{C}{4\sqrt{\pi}(\sigma^2 + \alpha^2 + \gamma^2)^{\frac{3}{2}}}.$$

Proof. By substituting $\eta = \sqrt{\sigma^2 + \alpha^2 + \gamma^2}$ in the identity

$$\int_{-\infty}^{\infty} \omega^2 e^{-\eta^2\omega^2} \mathrm{d}\omega = \frac{\sqrt{\pi}}{2\eta^3}, \tag{9}$$

we obtain

$$\Lambda(\sigma) = \frac{C}{2\pi} \int_{-\infty}^{\infty} \omega^2 e^{-(\sigma^2+\alpha^2+\gamma^2)\omega^2} \mathrm{d}\omega = \frac{C}{4\sqrt{\pi}(\sigma^2 + \alpha^2 + \gamma^2)^{\frac{3}{2}}}.$$

□

We also observe that the location d_0 of the maximum of Λ does not depend on α. This, of course, will be true in general.

Note that for the object function (8) the sharpness function

$$F(d) := \Lambda^{-2/3}(d - d_0), \tag{10}$$

is a quadratic polynomial

$$F(d) = \sqrt[3]{\frac{\pi}{C^2}}((d - d_0)^2 + \alpha^2 + \gamma^2).$$

It will be shown that in the general case the function $F(d)$ can be well approximated by a quadratic polynomial for suitable choices of the blur variable α. The quadratic shape of the sharpness function makes finding its optimum faster and more robust in the real-world applications.

4.2 Digital image object

In classical signal analysis a discrete signal ψ is modelled as a finite linear combination of delta functions (cf.[23])

$$\psi(x) = \sum_{k=1}^{K} a_k \delta(x - \mu_k), \quad a_k \geq 0. \tag{11}$$

In our setting, the finite sequence of numbers a_k are the pixel values located at $x = \mu_k$ of the one-dimensional object function, K is the number of pixels in the image. We consider an equally distributed set of pixels, so

$$\mu_k := k\tau, \quad \tau > 0. \tag{12}$$

The sampling period τ is known as the *pixel width.* We define the vector of pixel values

$$\mathbf{a} := (a_k)_{k=1}^{K}. \tag{13}$$

In this paper we consider the image with a finite number of pixels, i.e. $K < \infty$.

Proposition 1. *The power spectrum of the object function (11) can be expressed as*

$$|\hat{\psi}(\omega)|^2 = \sum_m \rho_m e^{im\tau\omega}, \tag{14}$$

where

$$\rho_m := \sum_l a_l a_{m+l} \tag{15}$$

are the autocorrelation coëfficiënts of the pixel values.

Proof. The Fourier transform of the object function (11)

$$\hat{\psi}(\omega) = \sum_k a_k \int_{-\infty}^{\infty} e^{-\mathrm{i}x\omega}\delta(x - k\tau)\mathrm{d}x = \sum_k a_k e^{-\mathrm{i}k\tau\omega}$$

is a periodic function with the period $\frac{2\pi}{\tau}$. Then its squared modulus $|\hat{\psi}(\omega)|^2$ is also a periodic function with period $\frac{2\pi}{\tau}$ having the Fourier expansion

$$|\hat{\psi}(\omega)|^2 = \sum_m \rho_m e^{\mathrm{i}m\tau\omega},$$

where

$$\rho_m = \frac{\tau}{2\pi}\int_{-\frac{\pi}{\tau}}^{\frac{\pi}{\tau}} |\hat{\psi}(\omega)|^2 e^{-\mathrm{i}m\tau\omega}\mathrm{d}\omega = \frac{\tau}{2\pi}\int_{-\frac{\pi}{\tau}}^{\frac{\pi}{\tau}} \overline{\hat{\psi}(\omega)} \sum_l a_l e^{-\mathrm{i}l\tau\omega} e^{-\mathrm{i}m\tau\omega}\mathrm{d}\omega =$$

$$\frac{\tau}{2\pi}\sum_l a_l \int_{-\frac{\pi}{\tau}}^{\frac{\pi}{\tau}} \overline{\hat{\psi}(\omega)} e^{-\mathrm{i}(l+m)\tau\omega}\mathrm{d}u = \sum_l a_l \bar{a}_{m+l} = \sum_l a_l a_{m+l}.$$

□

From definition (15) it trivially follows that

$$\sum_m \rho_m = \|\mathbf{a}\|_1^2. \tag{16}$$

Property 5. *The sharpness function* Λ *can be expressed by means of the autocorrelation coëfficiënts (15) as follows*

$$\Lambda(\sigma) = \frac{1}{2\pi(\sigma^2+\alpha^2)^{3/2}} \sum_m \rho_m \int_{-\infty}^{\infty} \omega^2 e^{\frac{im\omega\tau}{\sqrt{\alpha^2+\sigma^2}}} e^{-\omega^2} d\omega. \tag{17}$$

Proof. The proof is straight forward after we rewrite the sharpness function (6) for $\beta = 1$ as

$$\Lambda(\sigma) = \frac{1}{2\pi(\sigma^2+\alpha^2)^{3/2}} \int_{-\infty}^{\infty} \omega^2 |\hat{\psi}(\frac{\omega}{\sqrt{\alpha^2+\sigma^2}})|^2 e^{-\omega^2}\mathrm{d}\omega.$$

and substitute the expression for the power spectrum (14). □

In the two propositions below we approximate the sharpness function Λ by a function of the type $\frac{C}{(\alpha^2+\sigma)^{3/2}}$ in such a way that Λ can be written as

$$\Lambda(\sigma) = \frac{C}{(\alpha^2+\sigma^2)^{3/2}}(1 + R(\sigma)), \tag{18}$$

where C depends only on the pixel values $C = C(\mathbf{a})$ and a relative error R, which can be small in typical circumstances. This implies that the sharpness function (10) can be expressed as

$$F(d) = \mathcal{P}(d)(1 + \epsilon(d)),$$

where $\mathcal{P}$ is the second order polynomial. For a small error $R(\sigma)$, the relative error $\epsilon(d)$ will be small: $\epsilon(d) \doteq -\frac{2}{3}R(\sigma)$.

In practical applications the value of σ is important in relation to the pixel width τ. For instance if $\sigma \gg \tau$, the image is totally out-of-focus (for example, Figure 4(e)). It is often the case that $\sigma > \tau$, but not $\sigma \gg \tau$. However by controlling the blur α, the value $\sqrt{\alpha^2+\sigma^2}$ can be much greater than τ, which is important for our error analysis in the next propositions.

Proposition 2. *The sharpness function can be expressed as follows*

$$\Lambda(\sigma) = \frac{C_1}{2\pi(\alpha^2+\sigma^2)^{3/2}}(1 + R_1(\sigma)), \tag{19}$$

where

$$|R_1(\sigma)| \leq K_1 \frac{\tau}{\sqrt{\alpha^2+\sigma^2}}, \tag{20}$$

and C_1, K_1 *depend only on the pixel values* $\mathbf{a}$.

Proof. Splitting $e^{\frac{im\tau\omega}{\sqrt{\alpha^2+\sigma^2}}}$ into $(e^{\frac{im\tau\omega}{\sqrt{\alpha^2+\sigma^2}}} - 1) + 1$ in (17), one obtains

$$\Lambda(\sigma) = \frac{1}{2\pi(\sigma^2+\alpha^2)^{3/2}}(\underbrace{\int_{-\infty}^{\infty} \omega^2 e^{-\omega^2} \mathrm{d}\omega \sum_m \rho_m}_{C_1} + \int_{-\infty}^{\infty} \omega^2 e^{-\omega^2} \sum_m \rho_m (e^{\frac{im\tau\omega}{\sqrt{\alpha^2+\sigma^2}}} - 1)\mathrm{d}\omega). \tag{21}$$

Applying (16), and (9) for $\eta = 1$, one obtains

$$C_1 := \int_{-\infty}^{\infty} \omega^2 e^{-\omega^2} \mathrm{d}\omega \sum_m \rho_m = \frac{\sqrt{\pi}}{2} \|\mathbf{a}\|_1.$$

To estimate R_1 observe that

$$|e^{\mathrm{i}\eta} - 1| = 2|\sin\frac{\eta}{2}| \leq |\eta|, \quad \eta \in \mathbb{R}, \tag{22}$$

for $\eta = \frac{m\tau\omega}{\sqrt{\alpha^2+\sigma^2}}$, and consequentially

$$\Big|\sum_m \rho_m (e^{\frac{im\tau\omega}{\sqrt{\alpha^2+\sigma^2}}} - 1)\Big| \leq \Big(\sum_m |m|\rho_m\Big) \frac{|\omega|\tau}{\sqrt{\alpha^2+\sigma^2}}. \tag{23}$$

From the estimate (23) and $\int_{-\infty}^{\infty} |\omega|^3 e^{-\omega^2} \mathrm{d}\omega = 1$ it follows that

$$\Big|\int_{-\infty}^{\infty} \omega^2 e^{-\omega^2} \sum_m \rho_m (e^{\frac{im\tau\omega}{\sqrt{\alpha^2+\sigma^2}}} - 1)\mathrm{d}\omega\Big| \leq \Big(\sum_m |m|\rho_m\Big) \frac{\tau}{\sqrt{\alpha^2+\sigma^2}}.$$

Then the statement of the proposition is straight forward with

$$K_1 := \frac{2}{\sqrt{\pi}} \frac{\sum_m |m|\rho_m}{\sum_m \rho_m}$$

in (20).

□

It follows from the proposition that the sharpness function (10) can approximated by a quadratic polynomial at any accuracy by increasing the value of the blur α.

Imagine $\sigma \leq \tau$. It means that the image is almost in-focus and might be only slightly unsharp. Figures 4(a)-4(c) show the examples of artificially blurred images. From left to right: original image, blurred image with $\sigma/\tau = 0.5$, blurred image with $\sigma/\tau = 1$. We can hardly see any difference between original and blurred images. However, if we zoom into the details (figures 5(a)-5(c)) the difference is visible. This correspond to the fine focussing, which is considered in the proposition below.

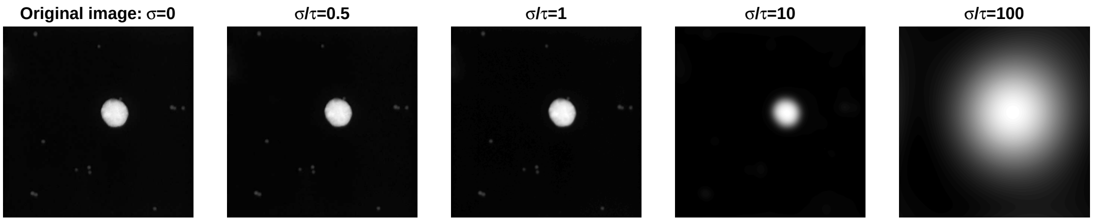

(a) (b) (c) (d) (e)

Figure 4: Artificially blurred images of a gold particle with different values of σ/τ.

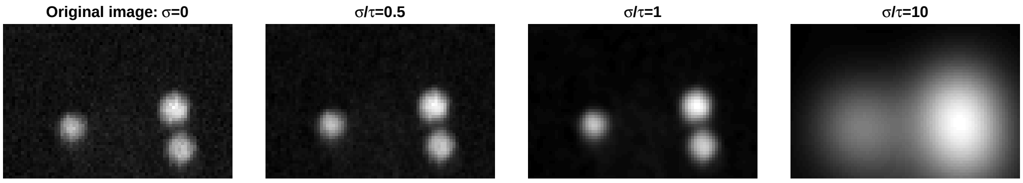

(a) (b) (c) (d)

Figure 5: Artificially blurred images of a gold particle with different values of σ/τ. The images are the magnified versions of those shown in Figure 4. Only if we zoom into the small particles we can see the difference in the image quality for the small values of σ.

Proposition 3. *The sharpness function can be expressed as follows*

$$\Lambda(\sigma) = \frac{C_2}{2\pi(\alpha^2+\sigma^2)^{3/2}}(1 + R_2(\sigma)), \tag{24}$$

where

$$|R_2(\sigma)| \leq K_2 \frac{\alpha^2+\sigma^2}{\tau^2}, \tag{25}$$

and C_2, K_2 depend only on the pixel values $\mathbf{a}$.

Proof. Splitting $\sum_m \rho_m$ into $\rho_0 + \sum_{m\neq 0} \rho_m$ in (17) one obtains

$$\Lambda(\sigma) = \frac{1}{2\pi(\sigma^2+\alpha^2)^{3/2}} \Big(\underbrace{\rho_0 \int_{-\infty}^{\infty} \omega^2 e^{-\omega^2} \mathrm{d}\omega}_{C_2} + \sum_{m\neq 0} \rho_m \int_{-\infty}^{\infty} \omega^2 e^{-\frac{im\tau\omega}{\sqrt{\alpha^2+\sigma^2}}} e^{-\omega^2} \mathrm{d}\omega \Big),$$

$$C_2 := \rho_0 \int_{-\infty}^{\infty} \omega^2 e^{-\omega^2} \mathrm{d}\omega = \frac{\sqrt{\pi}}{2} \|\mathbf{a}\|_2.$$

To estimate R_2 observe that

$$\Big| \int_{-\infty}^{\infty} \omega^2 e^{-\omega^2} e^{\mathrm{i}\eta\omega} \mathrm{d}\omega \Big| = \Big| \frac{\sqrt{\pi}}{4} (2-\eta^2) e^{-\frac{\eta^2}{4}} \Big| \leq \frac{4}{\eta^2}, \tag{26}$$

i.e. substitute $\eta = \frac{m\tau}{\sqrt{\alpha^2+\sigma^2}}$

$$\Big| \int_{-\infty}^{\infty} \omega^2 e^{-\omega^2} e^{\frac{im\tau\omega}{\sqrt{\alpha^2+\sigma^2}}} \mathrm{d}\omega \Big| \leq 4 \frac{\alpha^2+\sigma^2}{m^2\tau^2}.$$

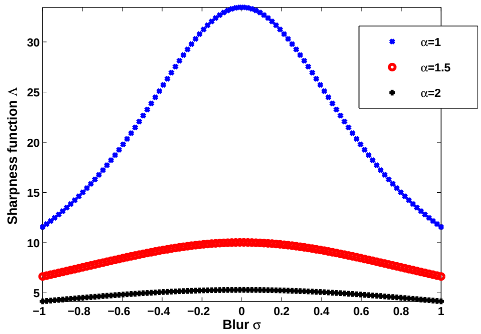

Figure 6: Sharpness function Λ computed for different values of the blur α.

Then the statement of the proposition is straight forward with

$$K_2 := \frac{8}{\sqrt{\pi}} \frac{\sum_{m \neq 0} \frac{\rho_m}{m^2}}{\rho_0}$$

in (25). □

Proposition 3 considers the situation of a very fine focussing, which is different from Proposition 2, where a more general case is considered. However it is shown that in both situations the sharpness function F can be approximated by a quadratic polynomial with a given accuracy. This coincides with findings of Property 4 for a different object function model.

5 The autofocus algorithm

It has been mentioned before that the function evaluations in our problem are very expensive and derivative information is not available. For this reason quadratic interpolation is a convenient approach for computing a quadratic polynomial approximation of the sharpness function. In our autofocus method we take the minimum of the polynomial as the minimum of the sharpness function. For the given data points $F_k := F(d_k), k = 1, 2, 3$ we interpolate the sharpness function F by a polynomial $\mathcal{P}(d) := c_0 + c_1 d + c_2 d^2$. So,one has

$$F(d) = \mathcal{P}(d)(1 + \epsilon(d)),$$

where $P(d_k) = F_k, k = 1, 2, 3$.

From Proposition 2 we conclude that the error $\epsilon(d)$ can be decreased by increasing α. Theoretically the error of this approximation (cf. Proposition 2) can be made as small as needed by dramatically increasing the value α. However, if $\alpha \to \infty$ then $F(d) \to 0$ and all its derivatives, which may causes numerical errors and make it difficult to find the optimum of the function. Figure 6 shows three sharpness functions computed for different α values. In the next section it will be shown how the large values of α influence the shape of the sharpness function computed for experimental through-focus series.

The above observations lead to the following **autofocus algorithm**:

1. Let d_2 be the current defocus control value of the optical device. Choose a Δd, then $d_1 := d_2 - \Delta d, d_3 := d_3 - \Delta d$.

Table 1: Overview of carbon cross grating experimental focus series.

N	Magnification	Pixel width τ [nm]	Defocus range $(d_N - d_1)$ [nm]	Defocus step Δd [nm]	Number of images N
1.	10 000 $\times$	42	36000	2000	19
2.	10 000 $\times$	42	10000	500	21
3.	200 000 $\times$	2.1	20000	1000	21
4.	200 000 $\times$	2.1	10000	500	21
5.	400 000 $\times$	1.05	900	50	19

2. Obtain three images at d_1, d_2, d_3 and compute F_1, F_2, F_3. We set $N = 3$.

3. We fit N given points with a quadratic polynomial for instance with the least squares and estimate d_{N+1}, the optimum of the quadratic polynomial.

4. If for the given tolerance $d_{tol} \in \mathbb{R}$, $|d_N - d_{N+1}| < d_{tol}$, stop. Else, compute $F_{N+1} = F(d_{N+1})$ and go to the previous step.

The parameter d_{tol} can be determined from the knowledge of the optical device behaviour. For instance, in electron microscopy the tolerable defocus error is defined as [33]

$$d_{tol} := \sqrt{(\frac{w}{2})^2 + (\frac{t}{2})^2},$$

where t is the object's thickness and w is the depth of field defined in [6] as

$$w := \frac{\tau}{\phi},$$

where ϕ is the *convergence semiangle* of the magnetic lens and τ is the pixel width. The tolerable defocus error can be considered as the lower bound set by the depth of field

$$d_{tol} = \frac{\tau}{2\phi}. \tag{27}$$

More steps ($N > 3$) of the method iterations are required only if a very accurate focusing is needed. The main goal of this paper is to try to estimate the in-focus image position from three or four recorded images. In the step three different numerical method could be used. The choice of the method is not quite significant for $N = 4$.

6 Numerical experiments with STEM images

Ten experimental through-focus series are obtained with the FEI STEM microscope. Two different samples are used: a carbon cross grating sample and a gold particle sample. Carbon cross grating is the standard sample for STEM calibration. The gold particle sample is a typical image example, used for particle analysis applications. The size of each image in the series is 512×512 pixels. The series are obtained at different magnifications and with different defocus steps. Figures 7-8 show the first image in the series, the in-focus image, and the computed sharpness function values plotted versus the values of defocus control. Each of the figures represent five series, described in the tables 1-2 (carbon cross grating sample and gold

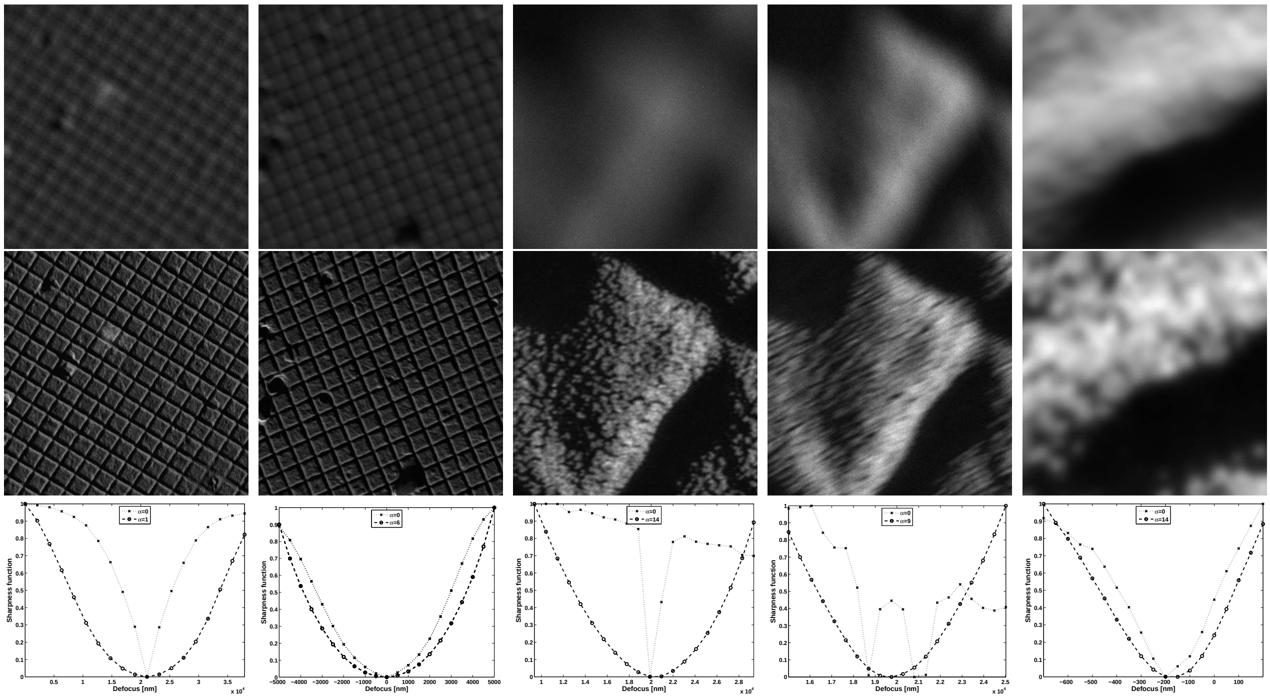

Figure 7: Sharpness functions computed for experimental STEM focus series of carbon cross grating sample. From top to bottom: The first image in the series, in-focus image from the series, sharpness functions with and without artificial blur plotted versus defocus. From left to right: Five different experimental focus series.

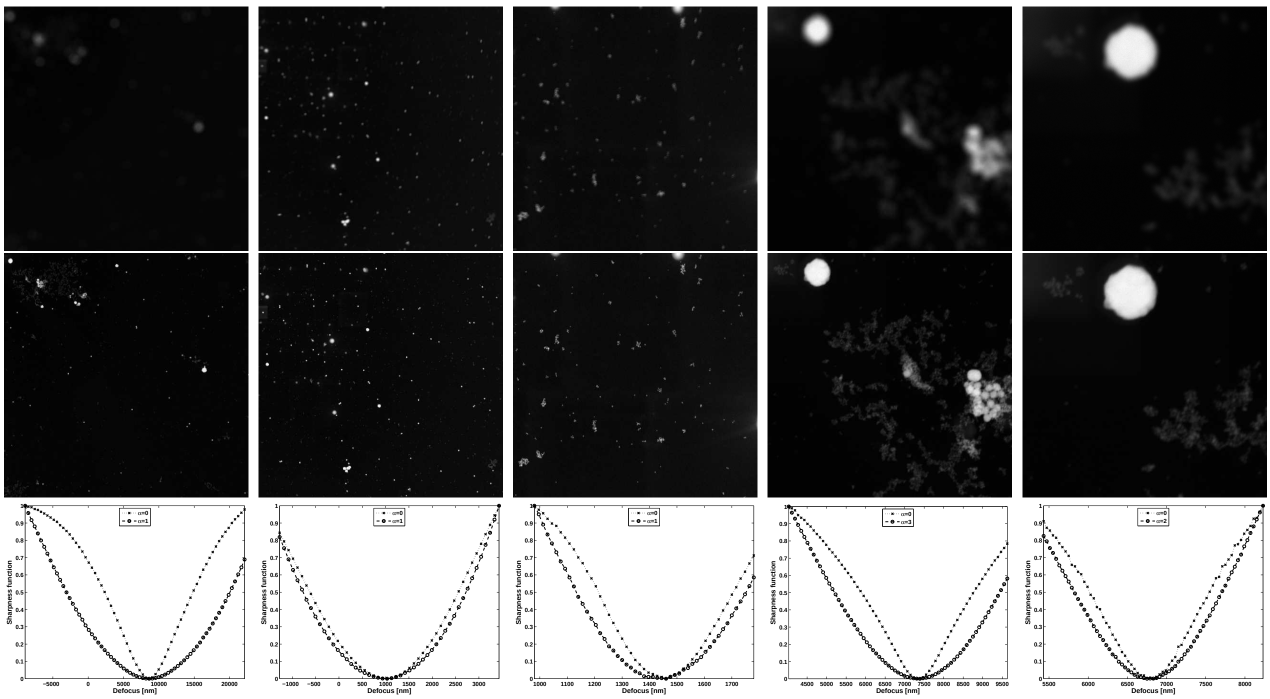

Figure 8: Sharpness functions computed for experimental STEM focus series of gold particles sample. From top to bottom: The first image in the series, in-focus image from the series, sharpness functions with and without artificial blur plotted versus defocus. From left to right: Five different experimental focus series.

Table 2: Overview of gold particles experimental focus series.

N	Magnification	Pixel width τ [nm]	Defocus range $(d_N - d_1)$ [nm]	Defocus step Δd [nm]	Number of images N
1.	10 000 $\times$	42	31500	450	70
2.	10 000 $\times$	42	4704	96	50
3.	56 000 $\times$	7.5	800	16	51
4.	56 000 $\times$	7.5	5600	80	71
5.	115 000 $\times$	3.75	2800	40	71

particles sample correspondingly). The line numbers in the tables N=1,2,3,4,5 correspond to the columns of the figures 7-8 (from left to right). For each series two functions are computed: with $\alpha = 0$ (dotted line) and with $\alpha > 0$ (dashed line). The values of both functions are scaled between 0 and 1. Computed derivative-based sharpness functions with $\alpha > 0$ can accurately be approximated with a quadratic polynomial.

The series shown in the second columns of figures 7-8 are recorded with a small defocus step. The qualities of the first image in the series and the in-focus image do not differ so much: We can see the details on the first images from the series, only the edges are a bit unsharp. It is shown in tables 1-2 (N=2) that these series have relatively small defocus ranges and defocus steps for particular magnification. For these cases the sharpness function has a shape nearly quadratic even with $\alpha = 0$, as follows from Proposition (3). The sharpness function shape is different in a broader defocus range for the same sample at the same magnification (Figure 7, first column and Figure 8, first column). The functions with $\alpha = 0$ have shapes similar to a Gaussian, but not a quadratic polynomial. In this case the functions have a nearly quadratic shape after applying the blur α to the images.

The fourth series of carbon cross grating (Figure 7, fourth column) is the only experimental series recorded with the presence of *astigmatism aberration*. For other experimental series astigmatism of the magnetic lens has been corrected before the recording. The lens with astigmatism is not perfectly symmetric and as a consequence has more than one focal point [22], which results in the asymmetry of the point spread function. Consequentially the recorded image cannot be totally sharp. The sharpness function might have local optima due to the presence of astigmatism [4, 28]. Two local minima can be seen in the plot. They disappear after applying the artificial blur.

In the last experiments (figures 7-8, fifth column) the magnification of the microscope is higher and as a consequence the influence of noise on the image quality increases. We can see that in these cases the blur α helps to cope with the noise in the sharpness function.

Figure 9 shows sharpness function F computed for different values of the blur α for experimental through-focus series of gold particles (N=1,2). For the large $\alpha = 20$ the function becomes noisy and does not provide useful information anymore. It follows that for the proper work of the method we have to make a proper choice of the value α, which is not too large, but also not too small. This choice might depend on the sample geometry as well as on the defocus range (how far away we are actually from the ideal d_0). The choice does not have to be made every time, but once for a particular application, where we deal with the class of geometrical objects. For all the runs of the method within the particle analysis application described in the next section the value of α if fixed $\alpha = 3$. The choice is made experimentally by computing the sharpness function for experimental data and fitting it with a quadratic polynomial. The value of α corresponding to the smallest approximation error is chosen.

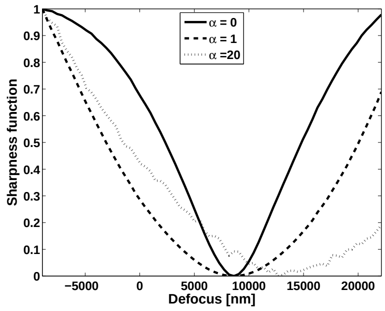

Figure 9: Sharpness function F computed for different values of the blur α for experimental through-focus series of gold particles (N=1,2), Table 2.

7 Application

The method is tested in a prototype FEI Tecnai F20 STEM electron microscope with the help of Java-based experimental platform (called EXPLA), which consists of a core that connects to the TEMScripting interface for FEI microscope control, and an application control framework [28]. For our experiment the autofocus method is implemented in Matlab V7.5 (R2007b). The method is integrated with a particle analysis application. The goal of this application is a statistical analysis of the particle distribution (particle locations and sizes). During the application run the images for further analysis are recorded at different positions and magnifications. During the run the position of the ideal defocus d_0 changes as the result of machine controls changes (stage position and magnification), as well as sample and environment instabilities. If the image is out-of-focus, the particle analysis software might give errors. For this reason it is important to run the algorithm of automated defocus correction with a certain periodicity in time as a part of particle analysis automated application.

Four examples of application runs are shown in Figure 10. The images of gold particles are focussed automatically. First two columns show autofocussing with three images, and the third and the fourth columns show autofocussing with four images. The recording of the fourth image might improve the final image quality (the sharpness function has a lower value). However, the improvement is not that strong. The difference between the fourth and the fifth resulting images in this experiment is not distinguishable by a human eye.

8 Discussion

The new method for rapid autofocussing is developed and tested for the reference case of scanning transmission electron microscopy. The tests are performed with the standard calibration sample and the particle analysis application. The algorithm is based on the general assumptions, and thus could be considered for other applications, such as electron tomography [33], as well as for other types of microscopes and different optical devices.

It has been proven that the derivative-based sharpness function is strictly monotone and has a unique optimum at the in-focus image for the noise-free image formation. This has already been used before on heuristic grounds in practical applications. The assumption of a Lévi point spread function is more general than a Gaussian point spread function used in a number of literature sources [4, 21, 38]. In a more general case the point spread function of a scanning transmission microscope could be modelled via the aberration function [13]. This assumption

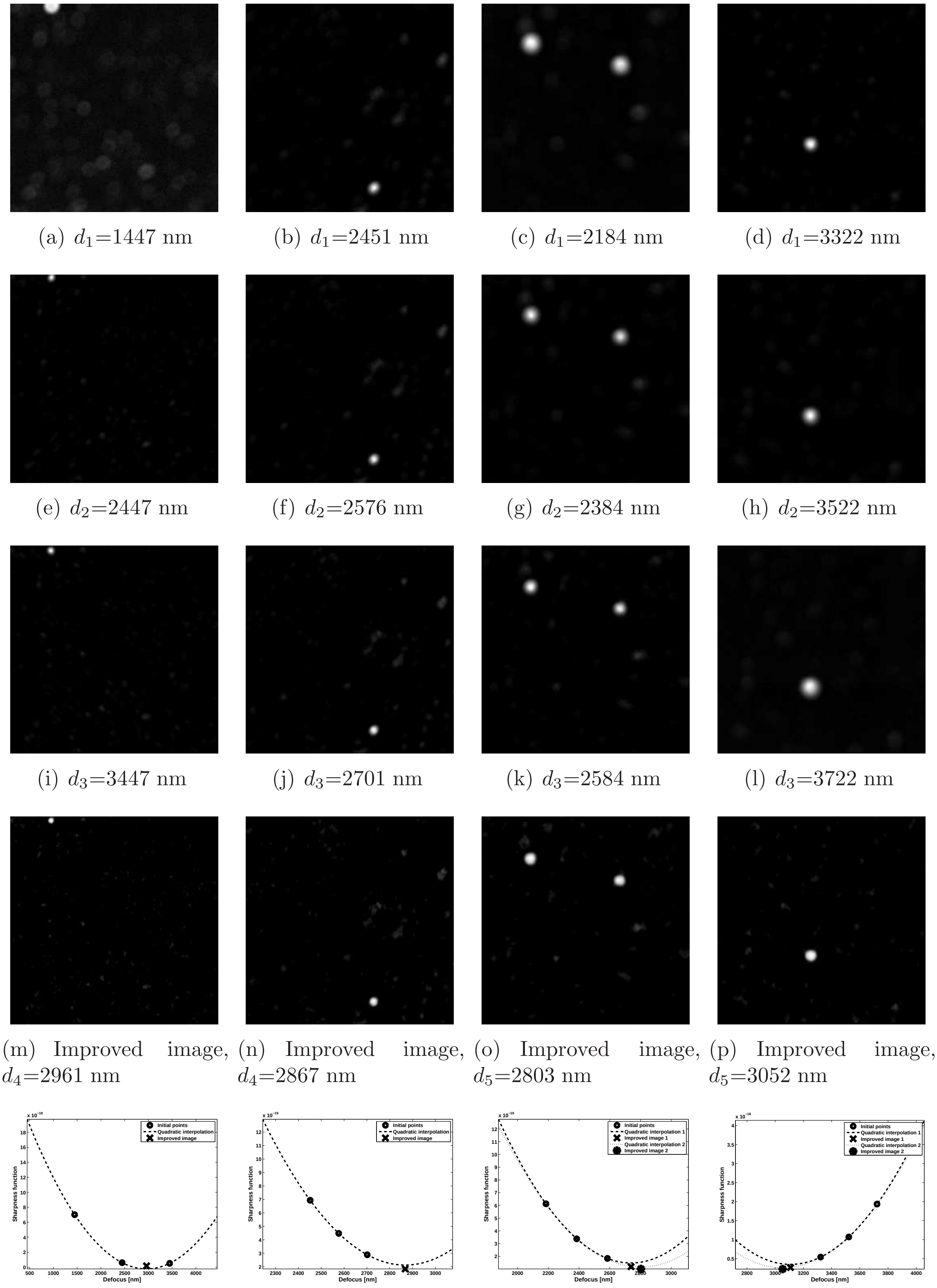

(a) d_1=1447 nm (b) d_1=2451 nm (c) d_1=2184 nm (d) d_1=3322 nm

(e) d_2=2447 nm (f) d_2=2576 nm (g) d_2=2384 nm (h) d_2=3522 nm

(i) d_3=3447 nm (j) d_3=2701 nm (k) d_3=2584 nm (l) d_3=3722 nm

(m) Improved image, d_4=2961 nm (n) Improved image, d_4=2867 nm (o) Improved image, d_5=2803 nm (p) Improved image, d_5=3052 nm

(q) (r) (s) (t)

Figure 10: On-line experiment: Image defocus improvement via interpolation the sharpness function by a quadratic polynomial.

makes the model difficult for analysis. In general case the sharpness function is not a quadratic polynomial. However, it has been shown that for the proper choice of the artificial blur α it can accurately be approximated by a quadratic polynomial. This provides the possibility of increasing the speed of the autofocus procedure.

The influence of noise, which is always present during the image formation in optical devices, on the sharpness function is not studied in this paper. We can see from numerical experiments with the real data as well as from the different papers [16, 28] that the noise in the image formation might result in the noise in the sharpness function, thus the function might obtain local optima and the statement of Property 1 is not true anymore. However, it is clear from numerical experiments with the real data and the on-line application runs that the sharpness function is nearly a quadratic polynomial for a reasonable amount of noise (the machine settings for recording the images are chosen in the same way as for the real-world applications). The artificial blur parameter α provides image smoothing that results in the smoothing of the sharpness function. The quantification of the influence of noise and the automated optimal choice of parameter α could be a topic of a research study in future.

Astigmatism aberration of the optical device lens results in the point spread function, which is not rotationally symmetric. This phenomenon has not been studied in this paper, because we have considered only one-dimensional setting. The presence of the astigmatism aberration might result in the multiple optima in a sharpness function [4, 27]. In one of the numerical experiments in this paper this effect has been shown. The influence of astigmatism on the sharpness function could be a topic of the future research. Moreover, by considering two-dimensional case the method might be extended to the simultaneous automated defocus and astigmatism correction method.

Appendix A

In this appendix we provide one more representation of the sharpness function with a different error estimates, which is controlled by $\frac{\sigma}{\alpha}$.

Proposition 4. *The sharpness function*

$$\Lambda(\sigma) = \frac{1}{2\pi(\sigma^2+\alpha^2)^{3/2}}\Big(\int_{-\infty}^{\infty}\omega^2|\hat{\psi}(\frac{\omega}{\alpha})|^2 e^{-\omega^2}d\omega + R_3(\sigma)\Big), \tag{28}$$

where

$$|R_3(\sigma)| \le (\sum_m |m|\rho_m)\frac{\tau}{\alpha}(\frac{\sigma}{\alpha})^2.$$

Proof. It is clear that in (28)

$$R_3 = \int_{-\infty}^{\infty}\omega^2(|\hat{\psi}(\frac{\omega}{\sqrt{\alpha^2+\sigma^2}})|^2 - |\hat{\psi}(\frac{\omega}{\alpha})|^2)e^{-\omega^2}\mathrm{d}\omega =$$

$$\int_{-\infty}^{\infty}\omega^2 e^{-\omega^2}\sum_m \rho_m(e^{\mathrm{i}m\tau\frac{\omega}{\sqrt{\alpha^2+\omega^2}}} - e^{\mathrm{i}m\tau\frac{\omega}{\alpha}})\mathrm{d}\omega.$$

Using (22), we obtain

$$|R_3| \le 2\int_{-\infty}^{\infty}\omega^2 e^{-\omega^2}\sum_m \rho_m\Big|\sin\frac{m\tau}{2}\omega(\frac{1}{\alpha} - \frac{1}{\sqrt{\alpha^2+\sigma^2}})\Big|\mathrm{d}\omega.$$

It is valid that

$$\frac{1}{\alpha} - \frac{1}{\sqrt{\alpha^2+\sigma^2}} = \frac{1}{\alpha\sqrt{1+(\frac{\sigma}{\alpha})^2}} \frac{(\frac{\sigma}{\alpha})^2}{1+\sqrt{1+(\frac{\sigma}{\alpha})^2}} \leq \frac{\sigma^2}{\alpha^3}.$$

Therefore,

$$|R_3| \leq \frac{\sigma^2\tau}{\alpha^3}\int_{-\infty}^{\infty}\omega^3 e^{-\omega^2}\sum_m |m|\rho_m \mathrm{d}\omega = (\sum_m |m|\rho_m)\frac{\tau}{\alpha}(\frac{\sigma}{\alpha})^2.$$

□

Appendix B

In the current appendix a different representation of the sharpness function is shown. The two corollaries below do not provide the prove, but give an intuitive feeling about the quadratic approximation of the sharpness function. They lead to the same conclusions as the propositions 3-2, which are more precise and contain the error estimates.

Property 6.

$$\Lambda(\sigma) = \frac{1}{8\sqrt{\pi}(\alpha^2+\sigma^2)^{3/2}}\sum_m \rho_m(2-\frac{m^2\tau^2}{\alpha^2+\sigma^2})e^{-\frac{1}{4}\frac{m^2\tau^2}{\alpha^2+\sigma^2}}. \tag{29}$$

Proof. Using the identity

$$\frac{1}{2\pi}\int_{-\infty}^{\infty}\omega^2 e^{-\omega^2}e^{\mathrm{i}\eta\omega}\mathrm{d}\omega = \frac{(2-\eta^2)e^{-\frac{\eta^2}{4}}}{8\sqrt{\pi}},$$

we obtain (29) straight forward from (17). □

The same representation as (29) is obtained via the matrix form in the theorem below.

Theorem 7. *For the object function (11)-(12) with a vector of amplitudes (13) and a linear image formation with a Gaussian point spread function the sharpness function (3) can be expressed as*

$$\Lambda(\sigma) = (\boldsymbol{\mathcal{A}}\mathbf{a}, \mathbf{a}), \tag{30}$$

where

$$\boldsymbol{\mathcal{A}} := (\mathcal{A}_{k,l})_{k,l=1}^K, \quad \mathcal{A}_{k,l} = \frac{1}{\sqrt{2\pi}(\sigma^2+\alpha^2)^{3/2}}(1-\frac{\tau^2(k-l)^2}{\sigma^2+\alpha^2})e^{-\frac{\tau^2(k-l)^2}{2(\sigma^2+\alpha^2)}}.$$

Proof. We express $\frac{\partial}{\partial x}(\psi * g_\sigma * g_\alpha)$ as a linear combination

$$\frac{\partial}{\partial x}(\psi * g_\sigma * g_\alpha) = \sum_k a_k g_k', \text{ where } g_k' := \frac{\partial}{\partial x}g_{\sqrt{\sigma^2+\alpha^2}}(x-\mu_k),$$

Then the norm can be expressed as

$$\|\frac{\partial}{\partial x}(\psi * g_\sigma * g_\alpha)\|_{L_2}^2 = \|\sum_k a_k g_k'\|_{L_2}^2 = (\sum_k a_k g_k', \sum_l a_l g_l') = \sum_{k,l}(g_k', g_l')a_k a_l = (\boldsymbol{\mathcal{A}}\mathbf{a}, \mathbf{a}),$$

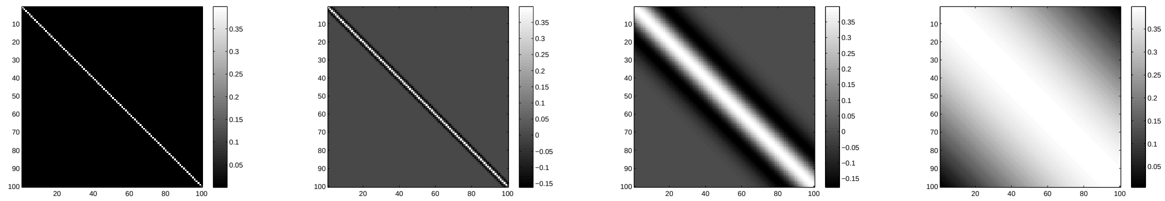

Figure 11: Density plots of matrix $\mathcal{A}$ computed for $\sqrt{\sigma^2+\alpha^2} = 1$ and the values $\tau = 10, 1, 0.1, 0.01$ (from left to right).

where

$$\mathcal{A}_{k,l} = (g'_k, g'_l).$$

For the Gaussian function we have $\frac{\partial}{\partial x} g = -\frac{\partial}{\partial \mu} g$. Hence,

$$(g'_k, g'_l) = \frac{\partial}{\partial \mu_k}\frac{\partial}{\partial \mu_l}\int_{-\infty}^{\infty} g_{\sqrt{\sigma^2+\alpha^2}}(x-\mu_k) g_{\sqrt{\sigma^2+\alpha^2}}(x-\mu_l)\mathrm{d}x,$$

which according to the Gaussian product property is

$$(g'_k, g'_l) = \frac{\partial}{\partial \mu_k}\frac{\partial}{\partial \mu_l} g_{\sqrt{\sigma^2+\alpha^2}}(\mu_k-\mu_l) = \frac{1}{\sigma^2+\alpha^2}(1-\frac{(\mu_k-\mu_l)^2}{\sigma^2+\alpha^2}) g_{\sqrt{\sigma^2+\alpha^2}}(\mu_k-\mu_l).$$

Further, for (12)

$$\mathcal{A}_{k,l} = \frac{1}{\sqrt{2\pi}(\sigma^2+\alpha^2)^{3/2}}(1-\frac{\tau^2(k-l)^2}{\sigma^2+\alpha^2})e^{-\frac{\tau^2(k-l)^2}{2(\sigma^2+\alpha^2)}}. \tag{31}$$

□

It follows from Theorem 7 that matrix $\mathcal{A}$ is symmetric, Toeplitz matrix, and it is positive-definite. The last property is a consequence of the fact that sharpness function Λ is defined as a norm. Hence, $(\mathcal{A}\mathbf{a}, \mathbf{a}) \geq 0$ for any $\mathbf{a}$. We denote $\mathcal{A}_k := \mathcal{A}_{k,1}$. We rewrite (30) as

$$\Lambda(\sigma) = \sum_k \sum_l a_k a_l \mathcal{A}_{k,l} = K\mathcal{A}_1 \sum_k a_k^2 + 2\sum_{n=2}^{N}(K+1-n)\mathcal{A}_n \sum_k a_k a_{k+1-n}.$$

In the following corollaries we consider two cases: 1) The matrix $\boldsymbol{\mathcal{A}}$ is close to diagonal; 2) the matrix $\boldsymbol{\mathcal{A}}$ is close to constant.

Corollary 8. *For $\sqrt{\sigma^2+\alpha^2} \ll \tau$ the matrix elements $\mathcal{A}_{k,l} \doteq 0$ for $k \neq l$, thus $\boldsymbol{\mathcal{A}} \doteq \frac{1}{\sqrt{2\pi}(\sigma^2+\alpha^2)^{3/2}}\boldsymbol{\mathcal{I}}$, where $\boldsymbol{\mathcal{I}}$ is identity matrix. As a consequence*

$$\Lambda(\sigma) = (\boldsymbol{\mathcal{A}}\mathbf{a}, \mathbf{a}) \doteq \frac{1}{\sqrt{2\pi}(\sigma^2+\alpha^2)^{3/2}}\|\mathbf{a}\|_2^2,$$

or for (10)

$$F(d) \doteq ((d-d_0)^2+\alpha^2)\sqrt[3]{2\pi\|\mathbf{a}\|_2^{-4}} \tag{32}$$

is a quadratic polynomial of defocus d.

This situation is illustrated in Figure 11. The density plot on the left is computed for $\sqrt{\sigma^2+\alpha^2}=1$ and $\tau=10$. The resulting matrix is nearly diagonal dominant. It means that close to the optimal defocus $d=d_0$ for small or zero α the sharpness function F can accurately be approximated by a quadratic polynomial.

Corollary 9. *For $\sqrt{\sigma^2+\alpha^2}\gg\tau$ the matrix elements $\mathcal{A}_{k,l}\doteq\frac{1}{\sqrt{2\pi}(\sigma^2+\alpha^2)^{3/2}}$, and as a consequence*

$$\Lambda(\sigma)=(\boldsymbol{\mathcal{A}}\mathbf{a},\mathbf{a})\doteq\frac{1}{\sqrt{2\pi}(\sigma^2+\alpha^2)^{3/2}}\|\mathbf{a}\|_1^2,$$

for (10)

$$F(d)\doteq((d-d_0)^2+\alpha^2)\sqrt[3]{\frac{2\pi}{\|\mathbf{a}\|_1^4}} \tag{33}$$

is a quadratic polynomial of defocus d.

This situation is illustrated in Figure 11. The density plot on the right is computed for $\sqrt{\sigma^2+\alpha^2}=1$ and $\tau=0.01$. In this case the matrix could be approximated with a constant and the sharpness function with a quadratic polynomial.

Acknowledgements

We kindly acknowledge R. Doornbos (ESI, The Netherlands) and S. Sluyterman (FEI, The Netherlands) for the recording of experimental data and on-line experiments, Wouter van den Broek (EMAT, Belgium) for providing experimental samples.

This work has been carried out as a part of the Condor project at FEI Company under the responsibilities of the Embedded Systems Institute (ESI). This project is partially supported by the Dutch Ministry of Economic Affairs under the BSIK program.

References

[1] J.F. Brenner, B.S. Dew, J. Brian Horton, T. King, P.W. Neurath, and W.D. Selles. An automated microscope for cytologic research a preliminary evaluation. J. Histochem. Cytochem., 24(1):100–111, 1976.

[2] A.S. Carasso. The APEX method in image sharpening and the use of low exponent levy stable laws. SIAM J. Appl. Math, 63(2):593–618, 2002.

[3] A.S. Carasso, D.S. Bright, and A.E. Vladar. APEX method and real-time blind deconvolution of scanning electron microscopy imagery. Opt. Eng, 41(10):2499–2514, 2002.

[4] S.J. Erasmus and K.C.A. Smith. An automatic focusing and astigmatism correction system for the SEM and CTEM. J. Microsc., 127(2):185–199, 1982.

[5] A. Erteza. Sharpness index and its application to focus control. Appl. Opt., 15(4):877–881, 1976.

[6] P.J. Goodhew, J. Humphreys, and R. Beanland. Electron microscopy and analysis. London : Taylor & Francis, 3rd ed. edition, 2001.

[7] J.W. Goodman. Fourier Optics. Roberts & Company, third edition edition, 2006.

[8] M. Haider, H. Muller, and S Uhlemann. Advances in imaging and electron physics, volume 153, chapter Present and Future Hexapole Aberration Correctors for High-Resolution Electron Microscopy, pages 43–120. Academic press, Amsterdam, The Netherlands, 2008.

[9] V. Hilsenstein. Robust autofocusing for automated microscopy imaging of fluorescently labelled bacteria. In Proc. International Conference on Digital Image Computing: Techniques and Applications, 2005.

[10] C.B. Johnson. A method for characterizing electro-optical device modulation transfer function. Photograph. Sci. Eng., 14(413–415), 1970.

[11] S. Jutamulia, T. Asakura, R.D. Bahuguna, and C. De Guzman. Autofocusing based on power-spectra analysis. Applied optics, 33(26):6210–6212, 1994.

[12] J. Kautsky, J. Flusser, B. Zitova, and S. Simberova. A new wavelet-based measure of image focus. Pattern recognition letters, 23:1785–1794, 2002.

[13] E.J. Kirkland. Advanced Computing in Electron Microscopy. Plenum Press, 1998.

[14] E. Krotkov. Focusing. Int. J. Comput. Vis., 1:223–237, 1987.

[15] T. Le, R. Chartrand, and T.J. Asaki. A variational approach to reconstructing images corrupted by poisson noise. J. Math. Imaging Vis., 27(3):257–263, 2007.

[16] X.Y. Liu, W.H. Wang, and Y. Sun. Dynamic evaluation of autofocusing for automated microscopic analysis of blood smear and pap smear. J. Microsc., 227:15–23, 2007.

[17] A.R. Lupini and S.J. Pennycook. Rapid autotuning for crystalline specimens from an inline hologram. J. Electon Microsc., 57(6):195–201, 2008.

[18] S. Morigi, L. Reichel, F. Sgallari, and A. Shyshkov. Cascadic multiresolution methods for image deblurring. SIAM J. Imaging Sci., 1(1):51–74, 2007.

[19] R.A. Muller and A. Buffington. Real-time correction of atmospherically degraded telescope images through image sharpening. J. Opt. Soc. Am., 64(9):1200–1210, 1974.

[20] K. Nakamae, M. Chikahisa, and Fujioka H. Estimation of electron probe profile from sem image through wavelet multiresolution analysis for inline sem inspection. Image. Vis. Comp., 25:1117–1123, 2007.

[21] S. K. Nayar and Y. Nakagawa. Shape from focus. IEEE Trans. Pattern Anal. Mach. Intell., 16(8):824–831, 1994.

[22] K.H. Ong, J.C.H. Phang, and J.T.L. Thong. A robust focusing and astigmatism correction method for the scanning electron microscope-part II: Autocorrelation-based coarse focusing method. Scanning, 20:324–334, 1997.

[23] A. Papoulis. Signal analysis. McGraw-Hill book company, 1977.

[24] P. Perona and J. Malik. Scale-space and edge detection using anisotropic diffusion. IEEE Trans. Pattern Anal. Mach. Intell., 12(7):629–639, 1990.

[25] M.E. Rudnaya, S.C. Kho, R.M.M. Mattheij, and J.M.L. Maubach. Derivative-free optimization for autofocus and astigmatism correction in electron microscopy. In Proc. 2nd International Conference on Engineering Optimization, Lisbon, Portugal, 2010.

[26] M.E. Rudnaya, R.M.M. Mattheij, and J.M.L. Maubach. Iterative autofocus algorithms for scanning electron microscopy. Microsc. Microanal., 15(Suppl 2):1108–1109, 2009.

[27] M.E. Rudnaya, R.M.M. Mattheij, and J.M.L. Maubach. Evaluating sharpness functions for automated scanning electron microscopy. J. Microsc., 240:38–49, 2010.

[28] M.E. Rudnaya, W. Van den Broek, R.M.P. Doornbos, R.M.M. Mattheij, and J.M.L. Maubach. Autofocus and two-fold astigmatism correction in HAADF-STEM. Ultramicroscopy, accepted, 2011.

[29] A. Santos, C.O. De Solórzano, J.J. Vaquero, J.M. Peña, N. Malpica, and F. Del Pozo. Evaluation of autofocus functions in molecular cytogenetic analysis. J. Microsc., 188:264–272, 1997.

[30] Y. Sun, S. Duthaler, and B.J. Nelson. Autofocusing in computer microscopy: Selecting the optimal focus algorithm. Microsc. Res. Tech., 65:139–149, 2004.

[31] N. Tanaka, J.J. Hu, and N. Baba. An on-linea correction method of defocus and astigmatism in HAADF-STEM. Ultamicroscopy, 78:103–110, 1999.

[32] A. Tejada, W. Van Den Broek, S. van der Hoeven, and A.J. den Dekker. Towards STEM control: Modeling framework and development of a sensor for defocus control. In Proc. 48th IEEE Conference on Decision and Control, pages 8310–8315, 2009.

[33] W. Van den Broek. Advanced Focus Methods in Electron Microscopy: Tomographic Reconstruction of the EELS Data Cube Autofocus of HAADF-STEM Images. PhD thesis, University of Antwerp, 2007.

[34] D. Vollath. Automatic focusing by correlative methods. J. Microsc., 147:279–288, Sep 1987.

[35] G. Yang and B.J. Nelson. Wavelet-based autofocusing and unsupervised segmentation of microscopic images. In Proc. of the Intl. Conference on Intelligent Robots and Systems, 2003.

[36] T.T.E. Yeo, S.H. Ong, Jayasooriah, and R. Sinniah. Autofocusing for tissue microscopy. Image Vis. Comput., 11(10):629–639, 1993.

[37] F. Zemlin, K. Weiss, W. Schiske, W. Kunath, and K.H. Herrmann. Coma-free alignment of high resolution electron microscopes with the aid of optical diffractograms. Ultramicroscopy, 3:49–60, 1978.

[38] Y. Zhang, Y. Zhang, and W. Changyun. A new focus measure method using moments. Image Vis. Comp., 18:959–965, 2000.

PREVIOUS PUBLICATIONS IN THIS SERIES:

Number	Author(s)	Title	Month
11-09	M.V. Ugryumova W.H.A. Schilders	Efficient simulation of power MOS transistors	Febr. '11
11-10	R. Rook	Notes on solving Maxwell equations Part 1: Finite elements method using vector elements	Febr. '11
11-11	R. Rook	Notes on solving Maxwell equations Part 2: Green's function for stratified media	Febr. '11
11-12	R. Mirzavand Boroujeni E.J.W. ter Maten T.G.J. Beelen W.H.A. Schilders A. Abdipour	Robust periodic steady state analysis of autonomous oscillators based on generalized eigenvalues	Febr. '11
11-13	M.E. Rudnaya H.G. ter Morsche J.M.L. Maubach R.M.M. Mattheij	A derivative-based fast autofocus method	Febr. '11

Ontwerp: de Tantes,
Tobias Baanders, CWI